

Contents lists available at ScienceDirect

Spectrochimica Acta Part A: Molecular and Biomolecular Spectroscopy

journal homepage: www.journals.elsevier.com/spectrochimica-acta-part-amolecular-and-biomolecular-spectroscopy





Dual-state emission, stretchability, information encryption, and intrinsic mechanism based on a butterfly shaped molecule

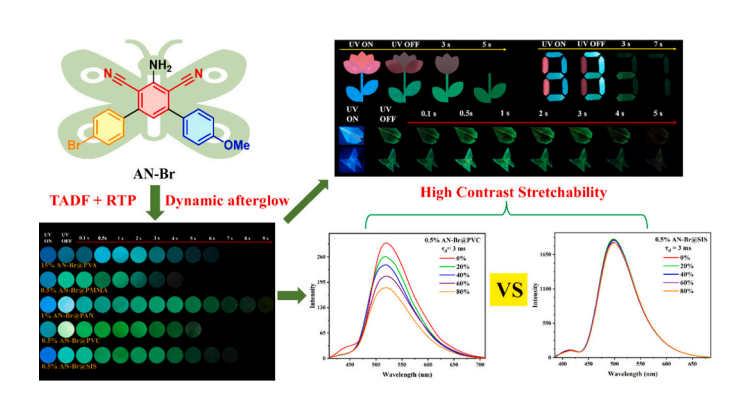
Weirao Ji^{a,1}, Meiling Pan^{b,1}, Jingjing Liu^a, Lei Ma^{b,c,d,*}, Yongtao Wang^{a,*}

- ^a College of Chemistry and Bioengineering, Guilin University of Technology, Guilin 541004, China
- ^b Tianjin International Center for Nanoparticles and Nanosystem, Tianjin University, Tianjin, 300072, China
- ^c Haihe laboratory for low dimensional electronic materials, Tianjin 300074, China
- ^d Tianjin Key laboratory of low dimensional electronic materials and advanced scientific instrumentation, Tianjin 300072, China

HIGHLIGHTS

- A butterfly-shaped molecule was constructed.
- The luminogen simultaneously possesses TADF and RTP emissions.
- · Strain sensing was achieved.
- Flexible and foldable materials with long afterglow were achieved.
- High-level information encryptions were successfully constructed.

G R A P H I C A L A B S T R A C T



ARTICLE INFO

Keywords: Thermally activated delayed fluorescence Room temperature phosphorescence Host-guest doping Strain detection Flexible phosphorescence

ABSTRACT

Flexible materials with dual-state emission, featuring thermally activated delayed fluorescence (TADF) and room-temperature phosphorescence (RTP), remain relatively rare, and the influence of different rigid and flexible doping matrices on the luminescence and stretchability properties of dual state emission luminogens are obscure. Here, a butterfly-shaped molecule named AN-Br was successfully prepared, presenting strong phosphorescence emission and dual-state emission in glassy THF and DMSO solutions respectively. By choosing different rigid and flexible doping matrices, luminescence and stretchability properties of AN-Br were investigated. The results demonstrated that AN-Br had similar dual-state emission in both rigid and flexible matrices, but with different RTP lifetimes ranging from 280.85 ms to 616.24 ms and afterglow durations from 4 s to 9 s, as well as time and temperature dependent dynamic afterglows. Notably, 0.5% AN-Br@PVC film presented obviously reduced RTP emission intensity and lifetime, as well as completely disappearing TADF emission with increasing strain, while 0.5% AN-Br@SIS film showed relatively stable RTP and TADF emission intensities and lifetimes. Moreover, 0.5% AN-Br@PVC and 0.5% AN-Br@SIS film exhibited excellent flexibility, especially for 0.5% AN-Br@SIS film with an elongation at break of 1000%. Long-lived red afterglow materials and high-level information encryptions were also achieved by constructing two ternary doping systems and leveraging the

^{*} Corresponding authors.

E-mail addresses: lei.ma@tju.edu.cn (L. Ma), wyt shzu@163.com (Y. Wang).

 $^{^{1}}$ Contributed equally.

distinct afterglow colors and durations. The work not only expands the application scope of dual-state emission materials in strain sensing but also elucidates the luminescence properties and underlying mechanisms of dual-state emission in various matrices, thereby advancing technological progress and innovative development of flexible dual-state emission materials.

1. Introduction

The excitons transition from the lowest singlet excited state (S₁) to the lowest triplet excited state (T₁) via intersystem crossing (ISC), then return to the ground state (S₀) through S₁ state, resulting in thermally activated delayed fluorescence (TADF) [1-6]. In contrast, phosphorescence involves the transition of excitons directly from the triplet excited state to the ground state. Theoretically, both TADF and roomtemperature phosphorescence (RTP) involve triplet excitons and compete with each other [7–9]. More importantly, RTP-type persistent luminescent materials experience increased non-radiative dissipation with rising temperature, leading to a significant decrease in afterglow lifetime and phosphorescence intensity, whereas TADF-type persistent luminescent materials exhibit an increase in luminescence brightness within a certain temperature range as the temperature rises, due to the accelerated thermal activation of excitons [10–13]. Therefore, persistent dual-state luminescent materials with TADF and RTP (TR) emission can exhibit temperature-dependent dynamic afterglow, which is beneficial for visual temperature sensing and complex encryption in anticounterfeiting materials [14-20]. Additionally, TADF and RTP typically have different radiative rates and sensitivities to oxygen, enabling TR emission materials to display time-dependent dynamic afterglow and hold promise for visual oxygen sensing. However, there are few reports on TR emission materials in visualizing strain sensing [21,22].

To enhance the luminescent properties of organic TR materials, researchers primarily employ strategies such as molecular structure optimization [23-27], crystal engineering [28-32], self-assembly [33,34], host-guest doping and so on [35-39]. Among these approaches, the host-guest doping strategy is considered highly advantageous due to its wide availability of materials and its ability to effectively regulate the microenvironment of luminescent materials [40]. This regulation optimizes energy transfer processes and luminescence efficiency while suppressing non-radiative transitions [41,42]. Despite the significant benefits of host-guest doping in improving luminescence performance, the investigation and application of TR luminescent materials in flexible matrices remain relatively limited. Flexible long afterglow materials can maintain excellent luminescence properties during bending and stretching, demonstrating superior mechanical flexibility and durability [43]. These characteristics make flexible long afterglow materials an ideal choice for wearable electronics and flexible display technologies [44]. They also offer vast potential for applications in material damage prediction, limb motion monitoring, smart clothing, and portable devices [45-47]. Therefore, developing flexible TR materials remains an important direction for current research [48,49]. However, flexible matrices generally lack strong intermolecular interactions (such as polar bonds), which exacerbate oxygen diffusion and non-radiative energy loss, thereby adversely affecting the stability of triplet excitons [49]. It is worth noting that, to date, there have been no reports in the literature on the changes in the intensity ratio and emission wavelengths of TADF and RTP emissions for TR luminescent materials under mechanical stretching of different flexible doping matrices.

In this paper, a butterfly-shaped molecule named AN-Br was successfully designed and synthesized. As a control, a linear molecule with a similar structure named BTDA was prepared. AN-Br showed phosphorescence nature in the glassy THF solution, presenting strong phosphorescence emission and long-lived green afterglow (11 s). In various doping matrices, including rigid matrices like poly(methyl methacrylate) (PMMA), poly(vinyl alcohol) (PVA), and polyacrylonitrile (PAN), as well as flexible matrices such as poly(vinyl chloride) (PVC) and

styrene-isobutylene-styrene block copolymer (SIS), AN-Br exhibited similar dual-state emission characterized by long-lived TADF and RTP. However, distinct time and temperature-dependent dynamic afterglows were observed. Most importantly, 0.5% AN-Br@SIS and 0.5% AN-Br@PVC films presented RTP lifetime of 502.11 ms and 363.52 ms, as well as afterglow duration of 7 s and 5 s in sequence, displaying excellent foldable and stretchable performance. Furthermore, 0.5% AN-Br@PVC film could be used as a potential visual strain detector, presenting completely disappearing TADF emission, obviously reduced RTP emission intensity and lifetime with increasing strain, but with relatively stable RTP and TADF emission intensities and lifetimes for 0.5% AN-Br@SIS film. Besides, long-lived red afterglow materials and highlevel information encryptions were achieved by constructing two ternary doping systems and leveraging the distinct afterglow colors and durations. It is worth mentioning that AN-Br shows significantly extended RTP lifetime and stronger afterglow compared to BTDA in different doping matrices due to reduced ISC and relaxation energy

2. Results and discussion

As shown in Fig. 1 and Scheme S1, a new butterfly-shaped luminogen named AN-Br was designed and synthesized by using methoxybenzene and bromodicyano benzidine as electron donor and electron acceptor respectively. By ¹H NMR, ¹³C NMR, HR-MS, and HPLC, its molecular structure and purity were characterized and confirmed (Figs. S15-S18). In n-hexane, the main absorption bands of the compound were located at 200–350 nm, corresponding to π - π * transition. In Tol, THF, and DMSO, the increased solvent polarity resulted in a new absorption band located at 350-425 nm, corresponding to the intramolecular charge transfer (ICT) state. Moreover, the absorption maxima of AN-Br at 350-425 nm showed continuous redshifts as the polarity of the solvent increased from Tol, THF, to DMSO. Compared to absorption maxima, fluorescence emission maxima of the luminogen gave more pronounced red shifts with increasing solvent polarity, corresponding to Stokes shifts of 42 nm (Fig. S1a and S1b). In diluted THF solution at 77 K, AN-Br had two emission maxima at 432 nm and 510 nm, emitting blue-green fluorescence under the irradiation of a 365-nm UV lamp. After ceasing the irradiation, AN-Br displayed green bright afterglow with phosphorescence emission maxima at 510 nm, lasting for 11 s (Fig. S1c and S1d). Notably, the fluorescence maxima of AN-Br at the low-energy level in the glassy THF solution precisely coincided with its phosphorescence maxima. This observation highlighted the dual-state emission characteristics of AN-Br and indicated a big ΔE_{ST} value (0.44 eV) between S_1 and T1 states. However, powder AN-Br showed invisible afterglow at room temperature (RT) due to molecular motions by turning on/off a 365 nm UV light lamp.

By crystal engineering, host-guest doping, supramolecular self-assembly, charge interactions, etc., suppressing molecular motion and isolating oxygen have become the important measure to achieve long-lived and efficient RTP. Secondly, PVA, and PMMA are the most commonly used host materials due to rigid structure and strong intermolecular hydrogen bonds. Therefore, a series of doping systems were constructed by using AN-Br and PVA/PMMA as guest and host materials respectively, whose RTP performance were optimized by altering the doping mass ratios between AN-Br and PVA/PMMA. Furthermore, different host-guest doping systems were named based on host and guest materials, as well as their doping mass ratio. For example, 15% AN-Br@PVA film was that AN-Br was doped into PVA matrix at the mass

ratio of 15:100 between AN-Br and PVA matrix. In various m% AN-Br@PVA films (m% is different mass ratio between AN-Br and PVA matrix), 15% AN-Br@PVA film presented the highest delayed emission intensity and the longest afterglow lifetimes (6 s) (Fig. S2). In comparison, the delayed emission peaks of 15% AN-Br@PVA film at 502 nm and 434 nm approached phosphorescence (510 nm) and fluorescence emission maxima (432 nm) of AN-Br in glassy THF solution respectively, speculating that 15% AN-Br@PVA film had simultaneously TADF and RTP of monomer AN-Br (Fig. S1d and S2d). In the phosphorescence excitation spectra, the spectral curves obtained with detection wavelengths at 434 nm and 502 nm showed a high degree of overlap, and both exhibited two main excitation peaks at 295 nm and 353 nm (Fig. S7c). This result indicates that the two emissions at 434 nm and 502 nm originate from two different excited states that transform into each other. The time-resolved delay spectra further confirmed the above speculation, presenting TADF and RTP lifetimes of 138.51 ms and 409.03 ms in sequence, as well as a subtle dynamic afterglow from blue to blue-green (Fig. 1c and d). The variable temperature phosphorescence spectra indicated that the emission intensity of the two peaks gradually decreased with the increase of temperature from 77 K to 297 K, but with stable emission maxima, confirming phosphorescence characteristics of the emission peak at 502 nm (Fig. S2b). However, TADF peak at 434 nm did not exhibit enhanced emission with increasing temperature, which might be due to self-quenching of TADF emission at high doping concentration. The elevated temperature may result in the reduced intermolecular distance, thereby enhancing self-quenching of TADF emission. Noteworthy, fluorescence emission maxima of 15% AN-Br@PVA showed significant redshifts than its TADF emission maxima at the same excitation wavelength (Figs. 1c and S2c). This is because high doping concentration leads to enhanced intermolecular interaction, which reduces the energy level of S₁ state, while TADF emission originates from AN-Br monomer. For m% AN-Br@PMMA films at different doping concentrations, 0.5% AN-Br@PMMA film showed the strongest RTP intensity, and the longest RTP (280.85 ms) and afterglow lifetimes (4 s) (Fig. 1b and c). In contrast, RTP and afterglow lifetimes of 0.5% AN-Br@PMMA film were shorter than that of 15% AN-Br@PVA film, indicating the significant influence of different host matrixes on luminescent properties of the guest material. Different from the dynamic afterglow of 15% AN-Br@PVA film, 0.5% AN-Br@PMMA film emitted constant green afterglow, with a single RTP peak at 510 nm, corresponding to phosphorescence emission of monomer AN-Br (Fig. 1b and c). By increasing decay time (τ_d) to 3 ms, 0.5% AN-Br@PMMA film also gave two emission peaks at 429 nm and 510 nm, corresponding to TADF and RTP emission in turn (Fig. 1c and d). Besides, 0.5% AN-Br@PMMA (light blue) and 15% AN-Br@PVA (deep blue) films presented high contrast fluorescence color. Fluorescence spectrum of the former simultaneously presented fluorescence and RTP emissions, located at 429 nm and 510 nm respectively, but with single fluorescence emission at 460 nm for the fluorescence spectrum of 15% AN-Br@PVA film (Figs. S2b and S3b), illustrating that AN-Br had a higher RTP radiation rate (K_p) in PMMA compared to in PVA. By expanding host material and optimizing doping mass ratio, RTP performance of AN-Br was further improved, and flexible TR emission materials and strain detection were achieved. 1% AN-Br@PAN film showed significantly prolonged RTP (616.24 ms) and afterglow (9 s) lifetimes, with TADF and RTP emission maxima at 429 nm and 507 nm respectively (Fig. 1b and d). Furthermore, TADF and RTP emission of 1% AN-Br@PAN film were confirmed by the variable temperature phosphorescence spectra (Fig. S4b). The emission intensity at 429 nm descended first then ascended, while emission intensity at 507 nm continually declined with the increase of temperature from 77 K to 297 K. Under a 365 nm UV lamp irradiation, 1% AN-Br@PAN film emitted blue fluorescence, whose fluorescence spectra also displayed dual state emission with TADF and RTP. Switching on/ off the 365 nm UV lamp, dynamic afterglow of 1% AN-Br@PAN film could be perceived from blue-green to yellow-green (Fig. S4a and S4c). Amazingly, AN-Br demonstrated outstanding RTP

performance in flexible PVC and SIS matrixes, especially for 0.5% AN-Br@PVC and 0.5% AN-Br@SIS films. By contrast, 0.5% AN-Br@PVC film presented shorter RTP (363.52 ms) and afterglow (5 s) lifetimes compared with 0.5% AN-Br@SIS films (502.11 ms and 7 s) (Fig. 1b and d). Similar to 0.5% AN-Br@PMMA film, 0.5% AN-Br@PVC film could not present dual-state emission with TADF and RTP until τ_{d} was extended to 3 ms, with constant green afterglow. However, 0.5% AN-Br@SIS film could show TADF and RTP emission at $\tau_d = 0$ ms, with TADF and RTP emission maxima of 415 nm and 499 nm in turn, as well as dynamic afterglow from blue to green (Fig. 1b and c). Thereby, whether there is a perceptible dynamic afterglow for the above doping films is related to τ_d when TADF can be detected. By contrast, 15% AN-Br@PVA, 1% AN-Br@PAN, and 0.5% AN-Br@SIS films possess long RTP lifetime, leading to immediately detectable TADF emission and the resulting dynamic afterglow. However, this is not the case for the 0.5% AN-Br@PVC and 0.5% AN-Br@PMMA films. As speculation, the short RTP lifetime of 0.5% AN-Br@PVC and 0.5% AN-Br@PMMA films means that the time for triplet excitons to stabilize in triplet state is relatively short, which are more likely to decay via non-radiative pathways or phosphorescence, thereby reducing the chances of reverse intersystem crossing (RISC). Of note, TADF (442 nm) and RTP (518 nm) maxima of 0.5% AN-Br@PVC film presented red shifts of 2-27 nm and 8-19 nm in turn compared with 15% AN-Br@PVA, 0.5% AN-Br@PMMA, 1% AN-Br@PAN, and 0.5% AN-Br@SIS films, which was not consistent with the polarity order of the five polymers (Fig. 1c). The chlorine atom effect might take responsibility for the above red shifted TADF and RTP emission, which allowed AN-Br to alter electron cloud distributions. For comparison, 0.5% AN-Br@PMMA film had the highest RTP (Φ_P) quantum vield, followed by 15% AN-Br@PVA, 1% AN-Br@PAN, 0.5% AN-Br@SIS, and 0.5% AN-Br@PVC films. Obviously, flexible matrix was not conducive to improving Φ_P , whose underlying reason should be the lower intersystem transition rate (K_{ISC}), rather than the increased non radiative phosphorescence rate (K_{nr}) (Table 1). For rigid doping matrices, high Φ_{P} and K_{nr} took responsibility for the short RTP and TADF lifetimes of 0.5% AN-Br@PMMA film, while 1% AN-Br@PAN film gave the smallest Φ_P and K_{nr} , leading to the longest RTP and TADF lifetimes (Table 1). Furthermore, 1% AN-Br@PAN film showed lower K_{nr} and higher K_{ISC} compared to 15% AN-Br@PVA and 0.5% AN-Br@PMMA films. However, Φ_P of 1% AN-Br@PAN film was lower than that of 15% AN-Br@PVA and 0.5% AN-Br@PMMA films, which was attributed to the small room temperature phosphorescence radiation rate (K_n) of 1% AN-Br@PAN film. In summary, AN-Br showed dual-band emissions with long-lived TADF and RTP in five doping matrixes, but with big ΔE_{ST} (0.39-0.50 eV), leading to weaker TADF emission compared with RTP. More importantly, AN-Br has long RTP and afterglow lifetimes in flexible PVC and SIS matrices. Such large ΔE_{ST} are not consistent with TADF-type luminogens reported in the literatures. What is the internal mechanism leading to the unusual dual state emission? Firstly, TADF and RTP lifetimes of luminogens with dual state emissions should show significant differences according to the triplet-triplet annihilation (TTET) mechanism, but they were close for 1% AN-Br@PAN film. Besides, the TTET process was usually very sensitive to temperature, and would be significantly enhanced at low temperature, because low temperature was conducive to the stability of the triplet excitons. However, 1% AN-Br@PAN and 0.5% AN-Br@SIS films gave TADF emission at 297 K rather than 77 K (Figs. S4b and S6b). Therefore, TADF of AN-Br did not come from the TTET process, but from AN-Br itself. Secondly, did TADF of the five doping films come from AN-Br monomers or aggregates? The variable temperature phosphorescence spectra of AN-Br in DMSO (10⁻⁵ M) indicated that TADF emission peak did not appear until the temperature increased to 227 K from 77 K, and TADF emission intensity further enhanced from 227 K to 257 K, thereby confirming AN-Br monomers with dual-state emissions (Fig. S7b). Based on the reverse temperature responses between TADF and RTP, four patterns were constructed by using 15% AN-Br@PVA, 0.5% AN-Br@PMMA, 1% AN-Br@PAN, and 0.5% AN-Br@PVC films respectively. Under 365 nm UV

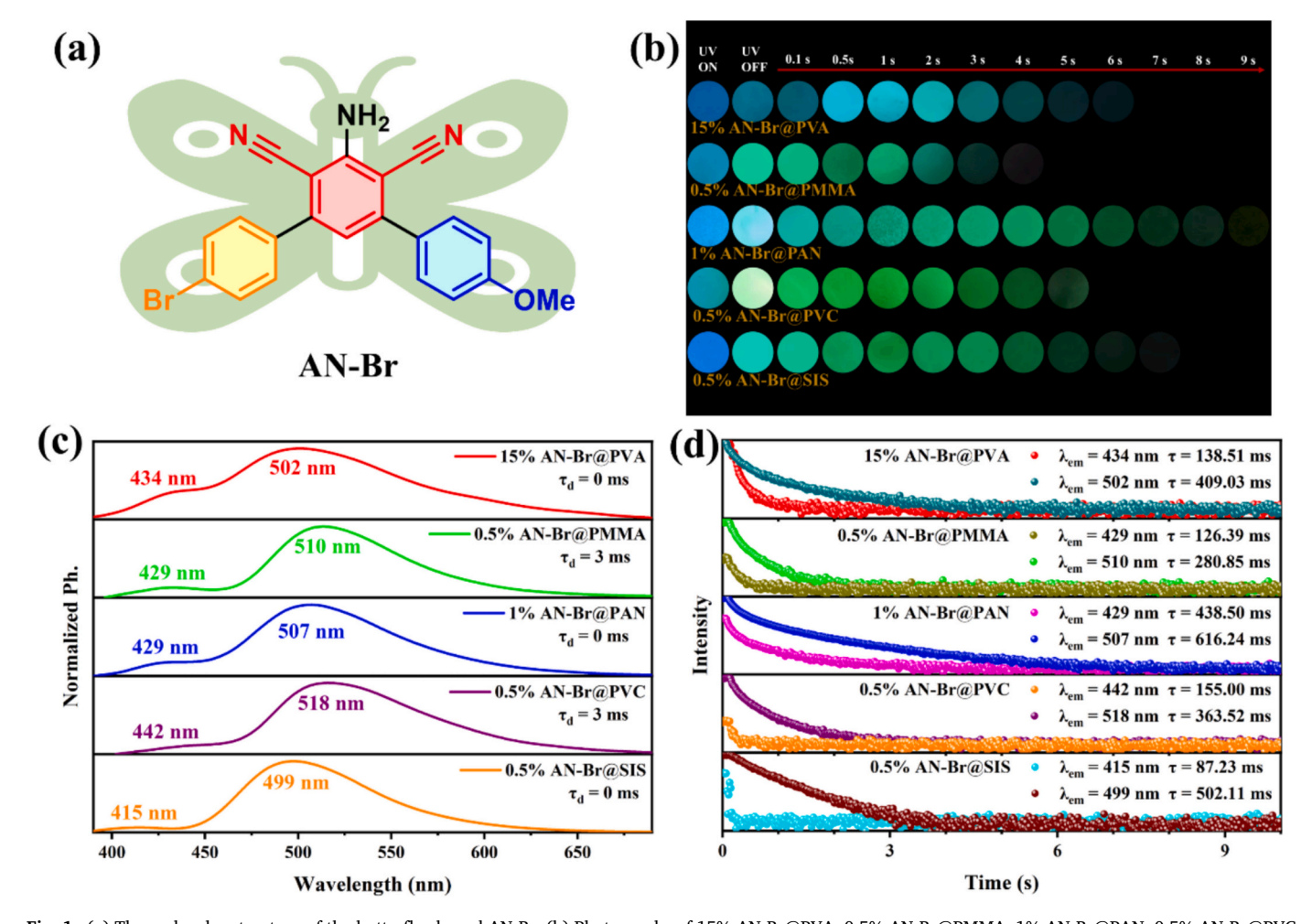


Fig. 1. (a) The molecular structure of the butterfly-shaped AN-Br; (b) Photographs of 15% AN-Br@PVA, 0.5% AN-Br@PMMA, 1% AN-Br@PAN, 0.5% AN-Br@PVC and 0.5% AN-Br@SIS films by turning on/ off a 365 nm UV light lamp; (c) The decay spectra of 15% AN-Br@PVA, 0.5% AN-Br@PMMA, 1% AN-Br@PAN, 0.5% AN-Br@PVC and 0.5% AN-Br@SIS films at different decay times (τ_d); (d) The time-resolved phosphorescent decay curves of 15% AN-Br@PVA, 0.5% AN-Br@PVA, 0.5% AN-Br@PMMA, 1% AN-Br@PAN, 0.5% AN-Br@PVC and 0.5% AN-Br@SIS films (τ_d : 0/3 ms, λ_{ex} : 365 nm).

irradiation, the four doping films emitted bright blue fluorescence at different temperatures. Upon switching off the 365 nm UV lamp, afterglow lifetimes and color changes of the four patterns were not significantly affected when the temperature increased from 0 $^{\circ}\text{C}$ to 25 $^{\circ}\text{C}$, but their afterglow lifetimes were dramatically reduced at 45 $^{\circ}\text{C}$. The comparison revealed that 1% AN-Br@PAN film exhibited the best stability and temperature responsiveness, with blue afterglow lasting for 2 s (Fig. S13). As a control, a linear molecule (BTDA) containing AN-Br partial structural units was designed and synthesized, whose afterglow was investigated under different doping matrices and concentrations. The results indicated that 5% BTDA@PVA film showed the longest afterglow lifetimes (3 s), followed by 1% BTDA@PVC film, but without visible afterglow in PAN and PMMA matrices (Fig. S14). The overall comparison displayed that AN-Br had longer RTP and TADF lifetimes, as

well as higher brightness than BTDA in four doping matrixes, confirming the effectiveness of molecular design strategies of AN-Br. The excellent dual-state emission of the doping systems was closely related to intermolecular interactions of host and guest materials. Thereby, corresponding binding energy and electrostatic interactions between AN-Br and five doping hosts were calculated (Figs. S11 and S12). For flexible matrices, the bonding energy between AN-Br and SIS is significantly higher than that between AN-Br and PVC. The intermolecular electrostatic interactions between AN-Br and SIS not only involve stronger hydrogen bonds but also van der Waals forces, whereas the interactions between AN-Br and PVC mainly come from van der Waals forces. The enhanced bonding energy and hydrogen bonding interactions lead to 0.5% AN-Br@SIS film exhibiting a lower K_{nr} compared to 0.5% AN-Br@PVC film. For rigid matrices, AN-Br has the biggest bond energy,

Table 1 Photophysical properties of various doping films.

| | λ _F (nm) | λ _P (nm) | $\tau_{\rm F}$ (ns) | τ _{TADF} (ms) | τ _P (ms) | Φ _F (%) | Φ_{TADF} (%) | $\Phi_{ m P}$ (%) | K_{TADF} (s^{-1}) | K_{ISC} (s^{-1}) | (s^{-1}) | (s^{-1}) | ΔE_{ST} (eV) |
|-----|------------------------|------------------------|---------------------|---------------------------|------------------------|-----------------------|----------------------------|-------------------|-----------------------|----------------------|------------|------------|----------------------|
| 1 | 450 | 502 | 3.26 | 138.51 | 409.03 | 1.22 | 1.19 | 4.24 | 0.09 | 3.03×10^8 | 0.10 | 2.34 | 0.39 |
| 2 | 429 | 510 | 2.18 | 126.39 | 280.85 | 8.98 | 2.23 | 5.82 | 0.09 | 4.18×10^8 | 0.23 | 3.33 | 0.46 |
| 3 | 429 | 507 | 1.86 | 438.50 | 616.24 | 11.28 | 1.53 | 3.74 | 0.04 | 4.77×10^8 | 0.07 | 1.55 | 0.44 |
| 4 | 456 | 518 | 3.50 | 155.00 | 363.52 | 3.05 | 0.66 | 1.75 | 0.04 | 2.77×10^8 | 0.05 | 2.70 | 0.41 |
| (5) | 447 | 499 | 2.88 | 87.23 | 502.11 | 15.62 | 0.36 | 2.93 | 0.05 | 2.93×10^{8} | 0.37 | 1.62 | 0.50 |

①: 15% AN-Br@PVA, ②: 0.5% AN-Br@PMMA, ③: 1% AN-Br@PAN, ④: 0.5% AN-Br@PVC, ⑤: 0.5% AN-Br@SIS.

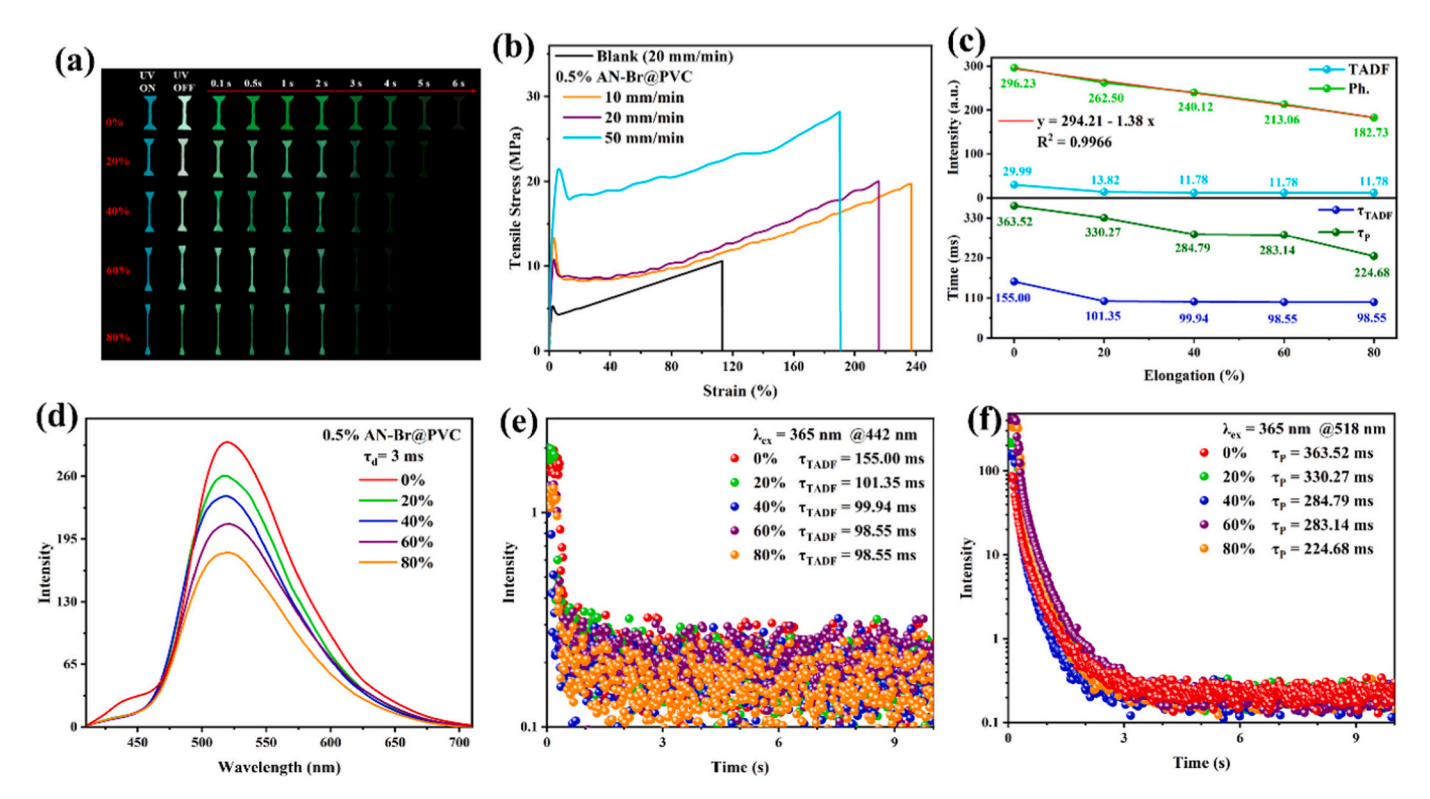


Fig. 2. (a) Photographs of 0.5% AN-Br@PVC stretching from original length 0% (2.0 cm) to 80% (3.6 cm) under 365 nm light irradiation; (b) Stress-strain curves of blank PVC film and 0.5% AN-Br@PVC film with a thickness of 0.158 mm and different tensile speeds (10, 20, and 50 mm/ min); (c) The variation tendency of RTP intensity and lifetime of 0.5% AN-Br@PVC film at different elongation; (d) Phosphorescence emission spectra of 0.5% AN-Br@PVC film stretching from original length 0% (2.0 cm) to 80% (3.6 cm); (e) – (f) The time-resolved TADF and RTP decay curves of 0.5% AN-Br@PVC film.

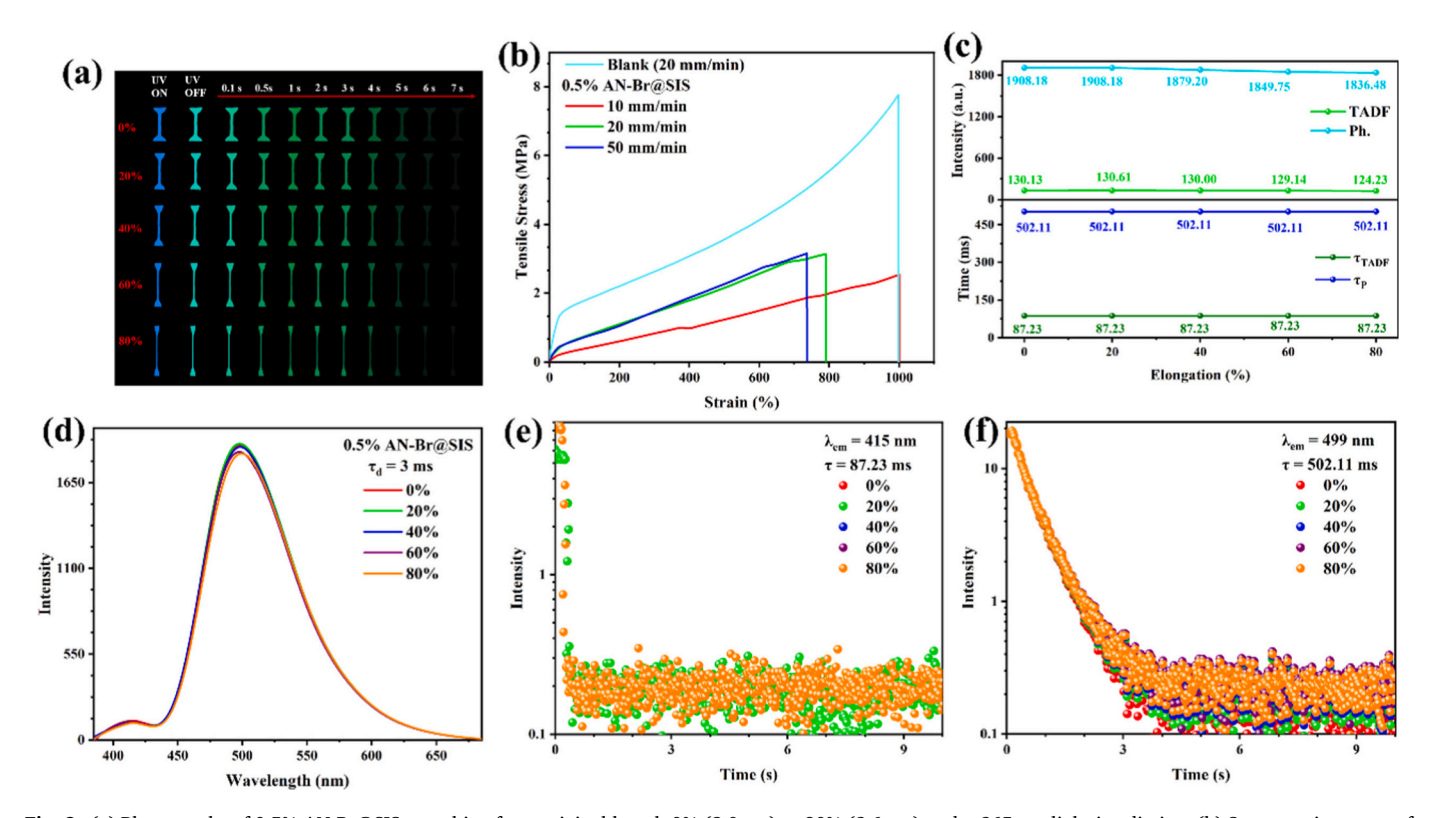


Fig. 3. (a) Photographs of 0.5% AN-Br@SIS stretching from original length 0% (2.0 cm) to 80% (3.6 cm) under 365 nm light irradiation; (b) Stress-strain curves of blank SIS film and 0.5% AN-Br@SIS film with a thickness of 0.668 mm and different tensile speeds (10, 20, and 50 mm/ min); (c) The variation tendency of RTP intensity and lifetime of 0.5% AN-Br@SIS film at different elongation; (d) Phosphorescence emission spectra of 0.5% AN-Br@SIS film stretching from original length 0% (2.0 cm) to 80% (3.6 cm); (e) – (f) The time-resolved TADF and RTP decay curves of 0.5% AN-Br@SIS film.

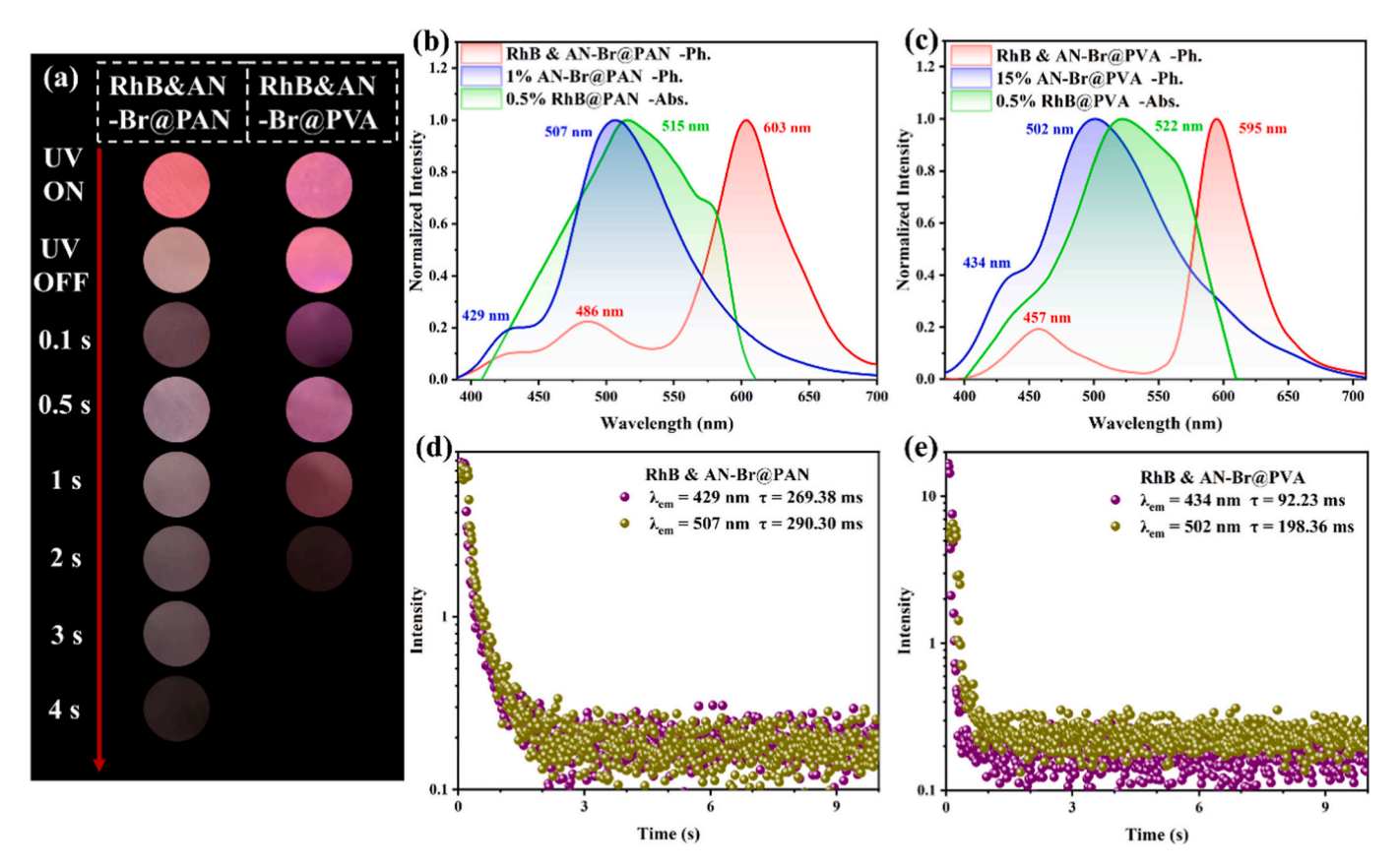


Fig. 4. (a) Photographs of RhB & AN-Br@PAN and RhB & AN-Br@PVA by turning on/ off a 365 nm UV lamp; (b) - (c) Normalized UV-vis absorption and fluorescence and phosphorescence emission spectra of RhB & AN-Br@PAN and RhB & AN-Br@PVA films; (d) - (e) The time-resolved phosphorescent decay curves of RhB & AN-Br@PAN and RhB & AN-Br@PVA films.

strong hydrogen bond and van der Waals interactions with PVA. Thereby, 1% AN-Br@PVA film gives smaller K_{nr} than 0.5% AN-Br@PMMA film. Despite weaker electrostatic interactions and very small bond energy, 1% AN-Br@PAN film shows the smallest K_{nr} . As shown in Table 1, 1% AN-Br@PAN film has a long RTP lifetime, which allows triplet excitons to persist for a longer duration before undergoing non-radiative decay, thereby resulting in relatively smaller K_p and K_{nr} .

To investigate the flexibility of the 0.5% AN-Br@PVC film, a series of uniaxial tensile tests were conducted (before the test, 0.5% AN-Br@PVC film was cut into a standard dumbbell shape, and the thickness was measured three times at different positions, with an average value of 0.158 mm). As shown in the stress-strain curve (Fig. 2b), the maximum tensile strength of the blank PVC film was 9.12 MPa at the tensile rate of 20 mm/min, and the maximum elongation at break was 109.17%. As the tensile rate increased from 10 mm/min to 50 mm/min, the tensile strength of 0.5% AN-Br@PVC film gradually increased to 19.91 MPa, 20.25 MPa, and 28.50 MPa, respectively, corresponding to the maximum stress of 4.22×10^3 kN, 4.96×10^3 kN and 6.14×10^3 kN, as well as the elongation at break of 237.16%, 215.63%, and 194.10%, respectively. At the same tensile rate (20 mm/min), the tensile strength and the elongation at break of the 0.5% AN-Br@PVC film were significantly higher than those of the blank PVC film (Fig. 2b), indicating that the host-guest doping between AN-Br and the PVC matrix could form more intermolecular interactions. Furthermore, the luminescent properties of 0.5% AN-Br@PVC film were investigated. When 0.5% AN-Br@PVC film was stretched to 3.6 cm from 2.0 cm, the corresponding RTP intensity decreased slowly, but with the stable RTP emission maxima. Of note, the TADF peak of 0.5% AN-Br@PVC film disappeared at elongation of 20-80%, which should be due to changes in molecular conformation during the stretching process (Fig. 2d). We know that TADF process involves reverse intersystem crossing (RISC) from T_1 to S_1 ,

which requires efficient intramolecular energy transfer. When stretching alters the molecular conformation of AN-Br, the above energy transfer efficiency is reduced, thereby decreasing emission intensity of TADF. However, the RTP peak is primarily determined by the electronic structure of AN-Br, and therefore it does not change. Meanwhile, RTP lifetime continuously decreased to 224.68 ms from 363.52 ms, corresponding to afterglow of 5 s and 4 s respectively. More importantly, RTP intensity and elongation showed a linear relationship (y = 294.21-1.38x, $R^2 = 0.9966$), which contributed to achieving visual strain detection (Fig. 2c). Similarly, 0.5% AN-Br@SIS film was cut into a standard dumbbell shape, and the thickness was measured three times at different positions, with an average value of 0.668 mm. As shown in Fig. 3b, the maximum tensile strength and elongation at break of the blank SIS film were 7.79 MPa and 997.46% in turn at a tensile rate of 20 mm/min. As the tensile rate increased from 10 mm/min to 50 mm/min, the elongation at break of 0.5% AN-Br@SIS films reached 1000.65%, 791.03% and 736.39%, respectively, corresponding to the maximum tensile strength of 2.55 MPa, 3.14 MPa, and 3.22 MPa, as well as the maximum fracture stress of 6.91 \times 10⁴ kN, 8.70 \times 10⁴ kN and 8.81 \times 10⁴ kN, respectively. By contrast, 0.5% AN-Br@SIS film showed extremely superior elongation at break and reduced tensile stress compared with 0.5% AN-Br@PVC film. At the same tensile rate (20 mm/ min), the tensile stress and elongation at break of 0.5% AN-Br@SIS film were lower than those of the blank SIS film. This can be attributed to the introduction of phosphorescent chromophores, which interfere with the normal arrangement and interaction of the SIS molecular chains, thereby reducing the material's overall mechanical properties. Different from 0.5% AN-Br@PVC film, RTP and TADF emission intensity and lifetime of 0.5% AN-Br@SIS film remained almost constant (Fig. 3d). PVC is a hard polymer with relatively rigid molecular chains, which lack the flexibility of SIS. During stretching, the interactions and stress

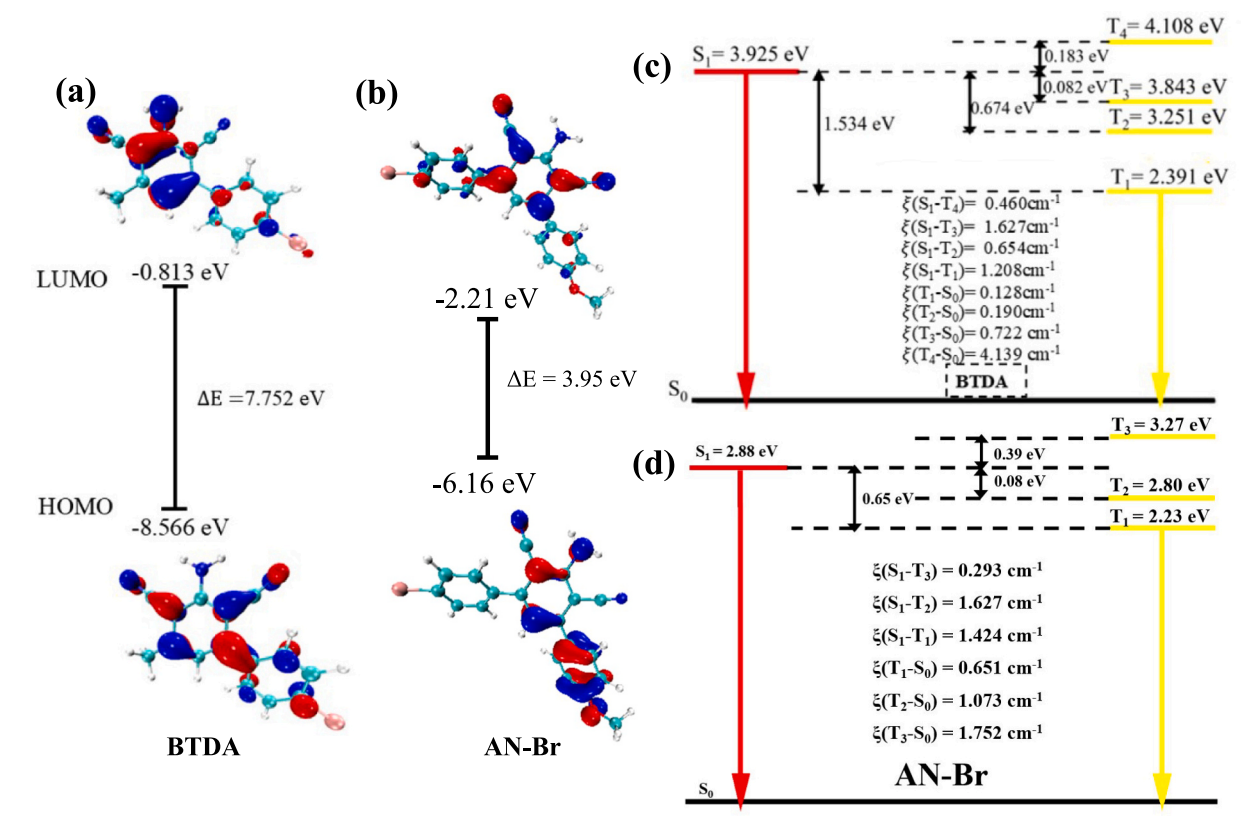


Fig. 5. (a) - (b) HOMO and LUMO distribution of BTDA and AN-Br; (c) - (d) Energy levels and spin orbit coupling constants (ξ) of BTDA and AN-Br.

distribution among PVC chains can alter the molecular environment of phosphorescent compounds, thereby affecting their luminescent properties. In contrast, SIS is a block copolymer with a flexible isobutene block that can absorb and disperse stress during stretching, reducing stress concentration and providing a more stable environment for phosphorescent compounds. Thereby, 0.5% AN-Br@PVC and 0.5% AN-Br@SIS films showed different luminescent stability.

Red and near-infrared afterglow materials exhibit strong tissue penetration and minimal damage to biological tissues, making them highly promising for applications in bioimaging and biosensing. However, these materials often suffer from enhanced non-radiative energy loss, which poses a significant challenge in developing highly efficient red and near-infrared afterglow materials. In recent years, Förster resonance energy transfer (FRET) theory and the heavy atom effect have played significant roles in the development of red and near-infrared materials. Thereby, two ternary doping systems named as RhB & AN-Br@PAN and RhB & AN-Br@PVA were constructed by using AN-Br and Rhodamine B (RhB) as FRET donor and acceptor in sequence, whose doping mass ratios were 0.5: 1: 100 between RhB, AN-Br and PAN, as well as 0.5: 15: 100 between RhB, AN-Br and PVA respectively. RhB & AN-Br@PAN film showed emission maxima (of 603 nm, RTP lifetime of 294.25 ms, afterglow of 4 s, and Φ_P of 0.07, while RhB & AN-Br@PVA film gave emission maxima of 595 nm, RTP lifetime of 210.07 ms. afterglow of 2 s. and, $\Phi_{\rm D}$ of 0.10. Compared to the 15% AN-Br@PVA film (with TADF and RTP FRET efficiencies of 0.33 and 0.52, respectively), the 0.5% RhB@1% AN-Br@PAN film exhibited higher TADF and RTP FRET efficiencies (0.39 and 0.53, respectively) (Table S1). This improvement was attributed to the better spectral overlap between the decay spectrum of the 1% AN-Br@PAN film and the UV-Vis absorption spectrum of RhB, compared to that between 15% AN-Br@PVA film and RhB (Fig. 4b and c). Notably, compared to 0.1 s after the UV lamp was turned off, the afterglow of two ternary doping systems was brighter at 0.5 s, which should be attributed to the delay in FRET (Fig. 4a).

The geometry optimizations of AN-Br were performed at the B3LYP/

def2-TZVP level using D4 dispersion correction, and all single-point calculations were performed at B3LYP/def2-TZVP level. The results indicated that the highest occupied molecular orbital (HOMO) of AN-Br was predominantly localized on the rest units except for bromobenzene, while the lowest unoccupied molecular orbital (LUMO) was mainly distributed over bromobenzene and dicyanodiamine moieties, demonstrating a pronounced intramolecular charge transfer (ICT) characteristic (Fig. 5a). The S₁ state energy level of AN-Br was 2.88 eV. Near the S₁ state, there existed three triplet states, T₁, T₂, and T₃, with energy gaps $(\Delta E_{ST}, \Delta E_{ST2}, \text{ and } \Delta E_{ST3})$ of 0.65 eV, 0.08 eV, and 0.39 eV, as well as the spin-orbit coupling constants (ξ) of 1.424 cm⁻¹, 1.627 cm⁻¹, and 0.293 cm⁻¹ between S₁ and T₁, T₂, T₃ respectively, indicating AN-Br had strong ISC ability. The experimental results and theoretical calculations both showed that AN-Br had a bigger ΔE_{ST} . Therefore, TADF emission of AN-Br should be attributed to the small ΔE_{ST2} and large ξ between S_1 and T₂ (Fig. 5d). By contrast, there were three triplet states levels (T₂, T₃, and T₃) near the S₁ state of BTDA, corresponding to energy gaps of 0.67 eV, 0.08 eV, and 0.18 eV, as well as ξ of 0.654 cm⁻¹, 1.627 cm⁻¹, and $0.460~{\rm cm}^{-1}$ in sequence, presenting ISC ability not weaker than AN-Br. However, the significantly increased ΔE_{ST} (1.53 eV) and ΔE_{T1T2} (0.886 eV) is not conducive to the formation of T1 triplet excitons for BTDA (Fig. 5c), leading to weaker RTP performance compared to AN-Br.

3. Application

Leveraging the distinct afterglow colors and durations, the outer and inner petals of the lotus were meticulously crafted using RhB & AN-Br@PVA and RhB & AN-Br@PAN films, respectively. The stems and leaves were fashioned from 1% AN-Br@PAN films. This setup dynamically mimicked the lifecycle of a lotus, from its vibrant bloom to its eventual withering, all accompanied by captivating color transitions. Under irradiation with a 365 nm UV lamp, the lotus displayed vivid red petals and striking blue stems and leaves. Upon switching off the UV lamp, a remarkable transformation occurred: the inner petals shifted

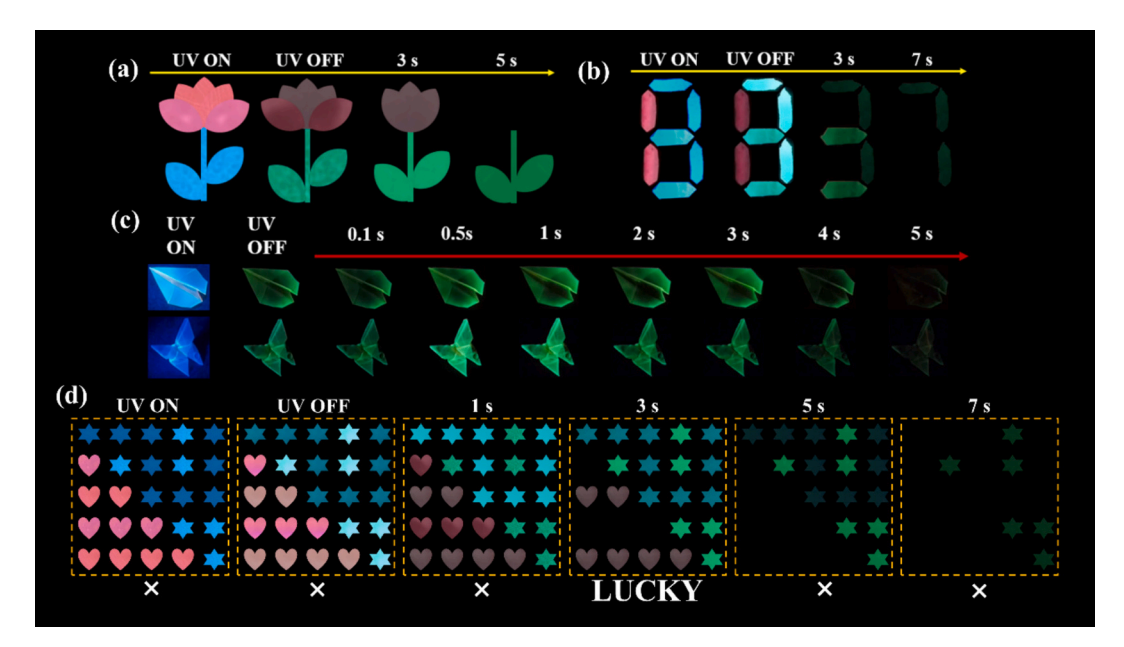


Fig. 6. (a) Graphic applications by RhB & AN-Br@PAN, RhB & AN-Br@PVA and 1% AN-Br@PAN; (b) Digital anti-counterfeiting by RhB & AN-Br@PVA, 0.5% AN-Br@PVC and 1% AN-Br@PAN; (c) Photographs of various large area, long-lasting and transparent art crafts prepared by stretching, folding, rolling, curling 0.5% AN-Br@PVC film under ambient conditions; (d) Alphabetic encryption by RhB & AN-Br@PAN, RhB & AN-Br@PVA, 15% AN-Br@PVA and 1% AN-Br@PAN.

from a bright red to a subdued red-gray hue, while the stems and leaves transitioned from blue to green. Within 1 to 5 s of turning off the lamp, the five petals of the lotus gradually withered away, illustrating the ephemeral beauty of this natural process (Fig. 6a). As depicted in Fig. 6b, a digital pattern illuminated by a 365 nm UV lamp showcased a dynamic display constructed from distinct afterglow materials. The red segments were meticulously crafted by cutting and assembling RhB & AN-Br@PVA film, while the blue segments were formed by cutting and assembling 0.5% AN-Br@PVC and 1% AN-Br@PAN films. Switching on/ off a 365 UV lamp, the afterglow properties of the materials came into play, revealing a sequence of numbers from "8" to "3" to "7" based on their emission durations. This not only demonstrated the potential for dynamic number display but also underscored the materials' utility in advanced encryption techniques. As illustrated in Fig. 6c, the threedimensional (3D) models of an airplane and a butterfly were fabricated by multiple twisting and folding 0.5% AN-Br@PVC films, indicating excellent flexibility. By switching on/off a 365 nm UV lamp, both 3D models exhibited a bright green afterglow, lasting for 5 s, which was akin to that of the pristine 0.5% AN-Br@PVC film. Finally, four types of the above doping films were selected to construct a series of heart and star patterns, which were then arranged in a 5×5 matrix. By turning on/ off a 365 nm UV lamp, the colors of heart and star patterns dynamically changed. Based on the distinct shapes and colors of the patterns in each row of the matrix, information encryption was achieved. Referring to a specific codebook (Fig. S10), when the UV lamp was turned off for 3 s, the matrix could be decrypted to read "LUCKY". At other time intervals, the matrix did not convey any meaningful information, thereby enabling complex dynamic information encryption (Fig. 6d).

4. Conclusion

A butterfly-shaped molecule named AN-Br was successfully synthesized, with strong phosphorescence emission and green afterglow in the glassy THF solution, lasting for 11 s. The luminogen exhibited TADF and RTP emissions in different polymer matrices and glassy DMSO solution, and with dynamic afterglow from blue to green for 15% AN-Br@PVA, 1% AN-Br@PAN, and 0.5% AN-Br@SIS films. Furthermore, 0.5% AN-Br@SIS and 0.5% AN-Br@PVC films presented RTP lifetimes of

502.11 ms and 363.52 ms, with corresponding afterglow durations of 7 s and 5 s, respectively, alongside outstanding foldable and stretchable mechanical properties. 0.5% AN-Br@PVC film could be used as strain detector, presenting reduced RTP emission intensity and lifetime with increasing strain, while 0.5% AN-Br@SIS film showed better stretchable performance compared with 0.5% AN-Br@PVC film, with elongation at break of 1000% at the tensile rate of 10 mm/min. At last, long-lived red afterglow and high-level information encryptions were successfully constructed. This research enriches pure organic persistent dual-state emission materials, achieves time/temperature-dependent dynamic afterglow, and expands their strain-sensing applications.

Declaration of competing interest

The authors declare that they have no known competing financial interests or personal relationships that could have appeared to influence the work reported in this paper.

Acknowledgment

This work was supported by the National Natural Science Foundation of China (Grant No. 22565012) and the Guangxi Natural Science Foundation (Grant No. 2024GXNSFAA999457).

Appendix A. Supplementary data

Supplementary data to this article can be found online at https://doi. org/10.1016/j.saa.2025.127139.

Data availability

I have shared all the data/code in the supporting information.

References

[1] K. Chen, Y. Jiang, Y. Zhu, Y. Lei, W. Dai, M. Liu, Z. Cai, H. Wu, X. Huang, Y. Dong, Host to regulate the T_1 – S_1 and T_1 – S_0 processes of guest excitons in doped systems to control the TADF and RTP emissions, J. Mater. Chem. C 10 (2022) 11607–11613, https://doi.org/10.1039/d2tc02167f.

- [2] R. Skaisgiris, T. Serevičius, K. Kazlauskas, Y. Geng, C. Adachi, S. Juršėnas, Origin of dual emission in σ-bridged donor-acceptor TADF compounds, J. Mater. Chem. C 7 (2019) 12601–12609, https://doi.org/10.1039/c9tc03548f.
- [3] R. Butkute, T. Serevicius, S. Raisys, K. Tulaite, L. Skhirtladze, G. Sini, J. V. Grazulevicius, S. Jursenas, Triplet harvesting in Trifluoromethyl Quinoxaline derivatives via TADF and RTP mechanisms, Opt. Mater. 158 (2025) 116421, https://doi.org/10.1016/j.optmat.2024.116421.
- [4] S.A. Elgadi, S. Mikulin, Z.M. Hudson, Recent Progress in organic TADF emitters containing heavy atoms, Adv Opt Mater 13 (2025) 2500683, https://doi.org/ 10.1002/adom.202500683.
- [5] T. Song, H. Liu, J. Ren, Z. Wang, Achieving TADF and RTP with stimulusresponsiveness and Tunability from phenothiazine-based donor-acceptor molecules, Adv Opt Mater 12 (2023) 2301215, https://doi.org/10.1002/ adom.202301215.
- [6] M. Li, W. Xie, X. Cai, X. Peng, K. Liu, Q. Gu, J. Zhou, W. Qiu, Z. Chen, Y. Gan, S. J. Su, Molecular engineering of sulfur-bridged polycyclic emitters towards tunable TADF and RTP electroluminescence, Angew. Chem. Int. Edit. 61 (2022) e202209343, https://doi.org/10.1002/anie.202209343.
- [7] M. Ferreira, N.O. Decarli, A. Nyga, K. Erfurt, J. Lingagouder, L.E. de Sousa, L. de Thieulloy, P. de Silva, P. Data, Multifunctional tris(triazolo)triazine-based emitter with dual-TADF, RTP, AIEE and AIDF properties, J. Mater. Chem. C 12 (2024) 13651–13664, https://doi.org/10.1039/d4tc00606b.
- [8] A. Vinod Kumar, P. Pattanayak, A. Khapre, A. Nandi, P. Purkayastha, R. Chandrasekar, Capturing the interplay between TADF and RTP through mechanically flexible polymorphic optical waveguides, Angew. Chem. Int. Edit. 63 (2024) e202411054, https://doi.org/10.1002/anie.202411054.
- [9] B. Zhou, Z. Qi, M. Dai, C. Xing, D. Yan, Ultralow-loss optical waveguides through balancing deep-blue TADF and Orange room temperature phosphorescence in hybrid antimony halide microstructures, Angew. Chem. Int. Edit. 63 (62) (2023) e202309913, https://doi.org/10.1002/anie.202309913.
- [10] X. Wang, J. Li, Y. Zeng, X. Chen, M. Wu, G. Wang, X. Li, B. Wang, K. Zhang, Merging thermally activated delayed fluorescence and two-photon ionization mechanisms for highly efficient and ultralong-lived organic afterglow, Chem. Eng. J. 460 (2023) 141916, https://doi.org/10.1016/j.cej.2023.141916.
- [11] Q. Mu, K. Zhang, H. Zou, H. Liu, Y. Song, C.-K. Wang, L. Lin, J. Fan, Theoretical insights into room temperature phosphorescence emission with anti-kasha behavior in aggregate, Dyes Pigments 205 (2022) 110560, https://doi.org/ 10.1016/j.dvenje.2022.110560.
- [12] Y. Hong, Y. Zhao, L. Ma, Y. Wang, Tuning triplet excitons and dynamic afterglow based on host-guest doping, Spectrochim. Acta A 324 (2025) 124955, https://doi. org/10.1016/j.saa.2024.124955
- [13] C. Yang, M. Pan, L. Ma, Y. Wang, Three in one: one host-guest doping system with mechanochromism, long afterglow, and thermally activated delayed fluorescence, Chem. Eng. J. 514 (2025) 163205, https://doi.org/10.1016/j.cej.2025.163205.
- [14] J.X. Wang, Y.G. Fang, C.X. Li, L.Y. Niu, W.H. Fang, G. Cui, Q.Z. Yang, Time-dependent afterglow color in a single-component organic molecular crystal, Angew. Chem. Int. Edit. 59 (2020) 10032–10036, https://doi.org/10.1002/anje.202001141
- [15] X. Bao, X. Zhu, Z. Tian, H. Wang, H. Li, X. Yuan, Dual-mode thermochromic afterglow in phosphorus-doped carbon dot composites for visible light-activated information encryption, J. Colloid Interface Sci. 690 (2025) 137331, https://doi. org/10.1016/j.jcis.2025.137331.
- [16] G. Liu, Z. Yan, Q. Song, Q. Sun, S. Xue, W. Yang, Pure organic thermally activated delayed fluorescence afterglow polymers via dopant isomerization, ACS Macro Lett. 14 (2025) 265–271, https://doi.org/10.1021/acsmacrolett.4c00818.
- [17] K. Kanosue, S. Ando, Polyimides with heavy halogens exhibiting room-temperature phosphorescence with very large stokes shifts, ACS Macro Lett. 5 (2016) 1301–1305, https://doi.org/10.1021/acsmacrolett.6b00642.
- [18] R.-J. Wei, X. Luo, G.-H. Ning, D. Li, Covalent metal-organic frameworks: Fusion of covalent organic frameworks and metal-organic frameworks, Acc. Chem. Res. 58 (5) (2025) 746–761, https://doi.org/10.1021/acs.accounts.4c00774.
- [19] S. Liu, Y. Lin, D. Yan, Dynamic multi-color long-afterglow and cold-warm white light through phosphorescence resonance energy transfer in host-guest metalorganic frameworks, Sci. China Chem. 66 (12) (2023) 3532–3538, https://doi.org/ 10.1007/s11426-023-1656-y.
- [20] F. Nie, D. Yan, Supramolecular glass: a new platform for ultralong phosphorescence, Sci. China Mater. 67 (11) (2024) 3531–3536, https://doi.org/ 10.1007/s40843-024-3119-5.
- [21] M. Wu, J. Li, J. Huang, X. Wang, G. Wang, X. Chen, X. Li, X. Chen, S. Ding, H. Zhang, K. Zhang, The unexpected mechanism of transformation from conventional room-temperature phosphorescence to TADF-type organic afterglow triggered by simple chemical modification, J. Mater. Chem. C 11 (2023) 2291–2301, https://doi.org/10.1039/d2tc05261j.
- [22] T. Li, N. Zhang, S. Zhao, M. Liu, K. Zhang, C. Zhang, J. Shu, T.-F. Yi, Long-lived dynamic room temperature phosphorescent carbon dots for advanced sensing and bioimaging applications, Coord. Chem. Rev. 516 (2024) 215987, https://doi.org/ 10.1016/j.ccr.2024.215987.
- [23] Y. Wang, M. Gao, J. Ren, J. Liang, Y. Zhao, M. Fang, J. Yang, Z. Li, Exciplex-induced TADF, persistent RTP and ML in a host-guest doping system, Mater. Chem. Front. 7 (2023) 1093–1099, https://doi.org/10.1039/d2qm01205g.
- [24] Q. Liao, Q. Gao, J. Wang, Y. Gong, Q. Peng, Y. Tian, Y. Fan, H. Guo, D. Ding, Q. Li, Z. Li, 9,9-Dimethylxanthene derivatives with room-temperature phosphorescence: substituent effects and emissive properties, Angew. Chem. Int. Edit. 59 (2020) 9946–9951, https://doi.org/10.1002/anie.201916057.

- [25] M. Dai, B. Zhou, D. Yan, Rare earth single-atomic hybrid glasses for near-infrared II optical waveguides, Angew. Chem. Int. Edit. 64 (27) (2025) e202505322, https://doi.org/10.1002/anie.202505322.
- [26] M. Dai, Z. Qi, D. Yan, In situ generation of microwire heterojunctions with flexible optical waveguide and hydration-mediated Photochromism, Angew. Chem. Int. Edit. 64 (7) (2024) e202420139, https://doi.org/10.1002/anie.202420139.
- [27] W. Zhou, M. Xu, X. Wang, X. Fang, X. Chen, Q. Kong, R. Zhang, L. Sun, L. Zhao, X. Lu, W.-Q. Deng, C. Liu, Three-dimensional interlocked crystalline frameworks for photocatalytic CO₂ conversion, CCS Chemistry 6 (12) (2024) 2866–2875, https://doi.org/10.31635/ccschem.024.202404171.
- [28] Z. Yin, Z. Wu, B. Liu, Recent advances in impurity-induced room-temperature phosphorescence, Adv. Mater. (2025) 2506549, https://doi.org/10.1002/ adma.202506549.
- [29] L. Shi, J. Liu, L. Ma, Y. Wang, The dual-band emission with long-lived thermally activated delayed fluorescence and room temperature phosphorescence by trace ingredient incorporation, Chem. Eng. J. 493 (2024) 152492, https://doi.org/ 10.1016/j.cej.2024.152492.
- [30] J. Guo, Y. Zhao, L. Ma, Y. Wang, Ultra-long room temperature phosphorescence, intrinsic mechanisms and application based on host-guest doping systems, Chin. J. Struct. Chem. 43 (2024), https://doi.org/10.1016/j.cjsc.2024.100335.
- [31] J. Jiang, J. Liu, C. Hu, Y. Wang, L. Ma, Construction and fine tuning of host-guest doping systems and the underlying mechanism of room temperature phosphorescence, Dyes Pigments 222 (2024) 111931, https://doi.org/10.1016/j. dyepig.2023.111931.
- [32] G. Yin, W. Lu, J. Huang, R. Li, D. Liu, L. Li, R. Zhou, G. Huo, T. Chen, Ultralong excimer phosphorescence by the self-assembly and confinement of terpyridine derivatives in polymeric matrices, Aggregate 4 (2023) e344, https://doi.org/ 10.1002/agt2.344.
- [33] H. Zheng, Z. Zhang, S. Cai, Z. An, W. Huang, Enhancing purely organic room temperature phosphorescence via supramolecular self-assembly, Adv. Mater. 36 (2024), https://doi.org/10.1002/adma.202311922.
- [34] Y. Zhu, M. Pan, W. Ji, L. Ma, Y. Wang, L. Ruan, Modulating room-temperature phosphorescence of Dπ-a luminogens via methyl substitution, positional isomerism, and host-guest doping, Spectrochim. Acta A 330 (2025) 125763, https://doi.org/10.1016/j.saa.2025.125763.
- [35] W. Ji, Y. Zhao, J. Guo, L. Ma, Y. Wang, Rapid construction and intrinsic mechanism of host-guest room temperature phosphorescence systems, Opt. Mater. 157 (2024) 116416, https://doi.org/10.1016/j.optmat.2024.116416.
- [36] J. Guo, C. Hu, J. Liu, Y. Wang, L. Ma, Mechanochromism, tunable pure organic room temperature phosphorescence, single-molecule near-white emission, digital encryption, and anti-counterfeiting, Dyes Pigments 221 (2024) 111760, https:// doi.org/10.1016/j.dvepig.2023.111760.
- [37] J. Li, S. Hao, M. Li, Y. Chen, H. Li, S. Wu, S. Yang, L. Dang, S.J. Su, M.D. Li, Triplet energy gap-regulated room temperature phosphorescence in host-guest doped systems, Angew. Chem. Int. Edit. 64 (2024) e202417426, https://doi.org/10.1002/anje.202417426.
- [38] L. Shi, X. Li, Y. Wang, L. Ma, Single component long-lived dynamic room temperature phosphorescence with large-scale preparation and visible light excitation, J. Mol. Struct. 1311 (2024) 138434, https://doi.org/10.1016/j. molstruc 2024 138434
- [39] J. Jiang, C. Hu, Y. Wang, L. Ma, J. Guo, Ultralong organic room-temperature phosphorescence, multiple stimulus responsiveness and high-level anticounterfeiting based on multifunctional carbazolyl imidazolopyridine, Mater. Today Chem. 30 (2023) 101548, https://doi.org/10.1016/j.mtchem.2023.101548.
- [40] L. Ma, X. Ma, Recent advances in room-temperature phosphorescent materials by manipulating intermolecular interactions, Sci. China Chem. 66 (2022) 304–314, https://doi.org/10.1007/s11426-022-1400-6.
- [41] J. Yang, M. Fang, Z. Li, Stimulus-responsive room temperature phosphorescence materials: internal mechanism, design strategy, and potential application, Acc. Mater. Res. 2 (2021) 644–654, https://doi.org/10.1021/accountsmr.1c00084.
- [42] Y. Zhu, M. Pan, L. Ma, Y. Wang, The luminescence mechanism of two pure organic room temperature phosphorescent isomers, mechanical force detection, 3D modeling, and dynamic data encryption, Chem. Eng. J. 505 (2025) 159245, https://doi.org/10.1016/j.cej.2025.159245.
- [43] Y. Zhu, H. Wu, M. Pan, L. Ma, Y. Wang, Achieving ultralong-lived flexible room-temperature phosphorescence, detection of strain and photostability, and high-level data encryption based on benzophenone derivatives, Chem. Eng. J. 519 (2025) 165087, https://doi.org/10.1016/j.cej.2025.165087.
- [44] J. Chen, F. Lin, D. Guo, T. Tang, Y. Miao, Y. Wu, W. Zhai, H. Huang, Z. Chi, Y. Chen, Z. Yang, In situ reversible and robust Mechano-responsive Ultralong phosphorescence of polyurethane elastomer, Adv. Mater. 36 (2024) 2409642, https://doi.org/10.1002/adma.202409642.
- [45] Y. Zhou, L. Jin, J. Chen, W. Hong, G. Liang, W. Qin, Five-in-one: dual-mode ultralong persistent luminescence with multiple responses from amorphous polymer films, Chem. Eng. J. 463 (2023) 142506, https://doi.org/10.1016/j. cei 2023 142506
- [46] H. Zhuang, A. Zhu, J. Jiang, W. Shi, H. Zhou, S. Hu, W. Bian, M. Li, X. Ban, Dendron-adhesive interlocking strategy for composite stretchable TADF film toward flexible OLED, Chem. Eng. J. 519 (2025), https://doi.org/10.1016/j. cei.2025.164942.
- [47] J. Zhang, J. Li, X. Li, S. Yuan, Y. Sun, Y. Zou, Y. Pan, K. Zhang, Boosting organic afterglow efficiency via triplet–triplet annihilation and thermally-activated

- delayed fluorescence, J. Mater. Chem. C 10 (2022) 4795–4804, https://doi.org/ 10.1039/d1tc04903h.
- [48] X. Han, X. Wang, Y. Wu, J. Zhao, Y. Liu, H. Shu, X. Wu, H. Tong, L. Wang, Modulation of triplet-mediated emission from selenoxanthen-9-one-based D-A-D Type emitters through tuning the twist angle to realize electroluminescence
- efficiency over 25%, J. Mater. Chem. C 10 (2022) 7437–7442, https://doi.org/ 10.1039/d2tc00899h.
- [49] G. Wang, J. Li, X. Li, X. Wang, Y. Sun, J. Liu, K. Zhang, Two-component design strategy: TADF-type organic afterglow for time-gated chemodosimeters, Chem. Eng. J. 431 (2022) 134197, https://doi.org/10.1016/j.cej.2021.134197.